

1 **$^2\text{H}/\text{H}$ and $^{18}\text{O}/^{16}\text{O}$ Non-Equilibrium Fractionation Factors for Ocean**
2 **Evaporation in the North-West Atlantic Region**

3 D. Zannoni¹, H. C. Steen-Larsen¹, A. J. Peters², S. Wahl¹, H. Sodemann¹ and A. E.
4 Sveinbjörnsdóttir³

5
6 ¹Geophysical Institute, University of Bergen and Bjerknes Centre for Climate Research, 5007,
7 Bergen, NORWAY.

8 ²Bermuda Institute of Ocean Sciences, St. George's GE01, BERMUDA.

9 ³Institute of Earth Sciences, University of Iceland, Reykjavik, ICELAND.

10
11 Corresponding author: Daniele Zannoni (daniele.zannoni@uib.no)

12
13 **Key Points:**

- 14 • Distributions of main water isotopologues' non-equilibrium fractionation factors for
15 evaporation in the North Atlantic Ocean are proposed.
16 • Significant correlation observed between non-equilibrium fractionation factors and 10-m
17 wind speed.
18 • Observed non-equilibrium fractionation factors agree only in part with the established
19 parametrization based on wind speed.
20 • No evidence of discontinuity in smooth and rough regimes for isotopic fractionation
21 during ocean evaporation.

22

23 Abstract

24 Isotopic evaporation models, such as the Craig-Gordon model, rely on the description of non-
 25 equilibrium fractionation factors that are, in general, poorly constrained. To date, only a few
 26 gradient-diffusion type measurements have been performed in ocean settings to test the validity
 27 of the commonly used non-equilibrium fractionation factor parametrizations for ocean
 28 evaporation. In this work we present six months of water vapor isotopic observations collected
 29 from a meteorological tower located in the northwest Atlantic Ocean (Bermuda) with the
 30 objective of estimating the best non-equilibrium fractionation factors (k , ‰) for ocean
 31 evaporation and their dependency on wind speed. Gradient-diffusion measurements are sensitive
 32 enough to resolve non-equilibrium fractionation factors during evaporation and provide mean
 33 values of $k_{18} = 5.2 \pm 0.6$ ‰ and $k_2 = 4.3 \pm 3.4$ ‰. In this study, we furthermore evaluate the
 34 relationship between k and 10-m wind speed over the ocean. Such relationship is expected from
 35 current evaporation theory and from laboratory experiments made in the 1970s, but observational
 36 evidence is lacking. We show that (i) sensitivity of k to wind speed is small, in the order of -0.16
 37 to 0.20 ‰ m^{-1}s for k_{18} , and (ii) there is no empirical evidence for the presence of a discontinuity
 38 between smooth and rough wind speed regime during isotopic fractionation, as proposed in
 39 earlier studies. Instead, k_{18} monotonically decreases within our observed wind speed range $[0 -$
 40 $10 \text{ m s}^{-1}]$. Implications for using such k values in modelling ocean vapor d-excess are briefly
 41 discussed.

43 Plain Language Summary

44 The theory behind non-equilibrium isotopic fractionation during ocean evaporation was
 45 formulated more than 50 years ago. However, still today there is little agreement on which are
 46 the best non-equilibrium fractionation factors to use in evaporation models. Currently, non-
 47 equilibrium fractionation factors are calculated following a parametrization based on wind speed
 48 experiments performed in the 1970s. This wind effect, which modulates the weight of molecular
 49 and turbulent transport of water vapor during evaporation has never been directly observed over
 50 the ocean. This study reports non-equilibrium fractionation factors for ocean evaporation
 51 estimated directly from flux measurements in an oceanic condition and explores their
 52 relationship with wind speed. Since having accurate fractionation factors is fundamental when
 53 modelling the Earth's water cycle with stable isotopes, the results of this study can help
 54 improving performances of General Circulation Models when describing ocean evaporation.

55 1 Introduction

56 Stable isotopes of hydrogen and oxygen in water have been used successfully for more
 57 than 50 years to study processes of the Earth's water cycle. Specifically, using water stable
 58 isotopes enables the atmospheric processes of the water cycle to be studied on time scales
 59 spanning mesoscale to glacial-interglacial time scales (Galewsky et al., 2016; Held & Soden,
 60 2000). Modulation of the water vapor isotopic composition, hereafter in delta notation, is linked
 61 to several physical processes occurring in the atmosphere and is considered a proxy for the
 62 atmospheric water vapor thermodynamic state. For instance, isotope ratios of $^{18}\text{O}/^{16}\text{O}$ ($\delta^{18}\text{O}$) and
 63 $^2\text{H}/\text{H}$ (δD) in precipitation are largely controlled by upstream cloud formation during moisture
 64 transport and isotopic equilibrium effect during phase changes (Craig, 1961; Dansgaard, 1964;
 65 Rozanski et al., 1993). On the other hand, the deviation from the linear relationship between
 66 $\delta^{18}\text{O}$ and δD (i.e., $\text{d-excess} = \delta\text{D} - 8 * \delta^{18}\text{O}$) in precipitation is controlled by one-directional non-
 67 equilibrium effects linked to evaporative conditions of moisture source areas (Craig & Gordon,

68 1965; Merlivat & Jouzel, 1979; S. Pfahl & Sodemann, 2014), by moisture recycling above the
 69 continents as well as by sub-cloud droplet evaporation (Risi et al., 2013; Stewart, 1975) and
 70 cloud microphysics (Ciais & Jouzel, 1994).

71 **1.1 Magnitude and control of non-equilibrium fractionation during ocean evaporation:** 72 **objectives of the study**

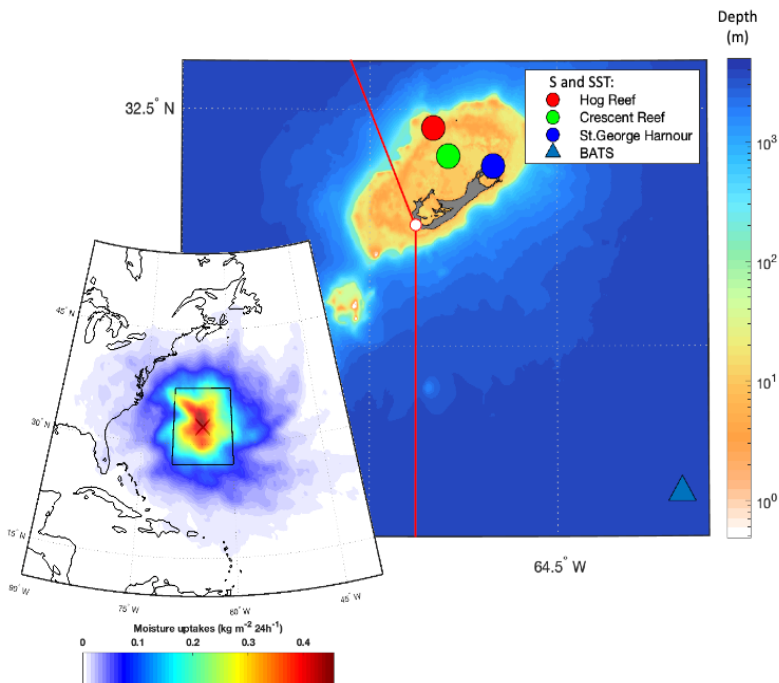
73 While isotopic fractionation effects during water phase changes in equilibrium conditions
 74 (above 0°C) are well understood, the non-equilibrium fractionation effects are still poorly
 75 constrained. During evaporation, a non-equilibrium process, the relative weight of molecular and
 76 turbulent diffusion controls the magnitude of non-equilibrium fractionation. While the values
 77 0.9757 and 0.9727 are in general considered representative for HD¹⁶O/H₂¹⁶O and H₂¹⁸O/H₂¹⁶O
 78 molecular diffusivity in air (Merlivat, 1978), their weights during natural evaporation were
 79 estimated to be only ~1/4 of a pure molecular diffusion controlled process (Horita et al., 2008).
 80 To this end, a largely adopted parametrization of non-equilibrium fractionation factors involves
 81 wind speed as the only independent variable (Merlivat & Coantic, 1975). However, several
 82 recent studies have questioned the assumed role of sea surface temperature (SST) and wind
 83 speed on the controls of non-equilibrium fractionation based on water vapor d-excess
 84 observations (Bonne et al., 2019; Steen-Larsen et al., 2014; Steen-Larsen et al., 2015; Uemura et
 85 al., 2008). Other studies argued that d-excess may not be influenced solely by ocean surface
 86 evaporative conditions, namely relative humidity (RH) and SST, but also by the Marine
 87 Boundary Layer (MBL) height and by the moisture input from the free troposphere (Benetti et
 88 al., 2018; Galewsky et al., 2022). Consequently, it can be concluded that a large uncertainty
 89 exists on the magnitude of non-equilibrium fractionation during evaporation in real-
 90 environmental conditions and, still, no agreement exists on the controls of non-equilibrium
 91 fractionation by SST and wind speed (e.g. Gonfiantini et al., 2020). This lack of consensus drives
 92 the following questions: which non-equilibrium fractionation factors are the most accurate to use
 93 during the evaporation process in the marine boundary layer? Is there empirical evidence for a
 94 dependency between non-equilibrium effects and wind speed in the oceanic environment? If a
 95 relationship between wind speed and non-equilibrium fractionation exists, is it captured by
 96 established parametrization based on wind tunnel experiments? And finally, what is the impact
 97 of MBL structure, ocean isotopic composition and SST variability on the estimation of
 98 evaporation flux composition during natural evaporation over the ocean? These research
 99 questions will be addressed in this study by:

- 100 1. Estimating the best non-equilibrium fractionation factors for $\delta^{18}\text{O}$ and δD that can
 101 explain the observed isotopic composition of evaporation flux from the ocean surface.
- 102 2. Test the validity of theoretical parametrization of the wind speed effect on non-
 103 equilibrium fractionation with observations of the isotopic composition of evaporation
 104 flux over the ocean.
- 105 3. Test the sensitivity of observed non-equilibrium fractionation factors against ocean
 106 isotopic composition and SST variability.

107 Furthermore, we discuss the implications for using the estimated non-equilibrium fractionation
 108 factors when modelling ocean vapor d-excess and how the height of MBL can explain a
 109 significant portion of the water vapor d-excess variability in the study area.

111 1.2 The problem of evaporation flux representativity in the isotopic composition of near- 112 surface water vapor

113 In general, links between ocean conditions, non-equilibrium fractionation and d-excess
114 are based on the assumption that observations of the d-excess signal in atmospheric water vapor
115 are representative of local evaporation in steady state. This assumption, however, is no longer
116 valid when measurements are performed in low evaporation areas or for periods when other
117 prevailing water vapor exchange processes, such as advection, occur in the atmosphere.
118 Therefore, the wind speed effect could be smoothed out in vapor d-excess signal by other
119 processes. Observations of water vapor isotopic composition at a single height level then might
120 not be representative of the evaporation flux. Instead, profile observations of water vapor
121 isotopic composition in ocean settings are particularly beneficial to estimate the isotopic
122 composition of the evaporation flux. Many profile measurements are available in continental
123 settings from atmospheric research and flux towers (e.g. Griffis et al., 2016) but such type of
124 measurements is scarce for the ocean. Most of the available profile observations over the ocean
125 were acquired for short time frames with low-temporal resolution techniques in the past (Gat et
126 al., 2003; Craig & Gordon, 1965). More recently, two-heights profiles were acquired during
127 cruises but introducing some additional uncertainties due to the use of different instruments for
128 isotopic analysis at each height, ship movement, ship exhaust and ocean spray contribution to the
129 vapor composition (Thurnherr et al., 2020). In this study we analyze six months (20th June to 30th
130 December 2013) of continuous observations of water vapor isotopic composition sampled at two
131 heights from a meteorological tower located in the northwest Atlantic region (Bermuda, Figure
132 1).



133

134 **Figure 1:** Study site of water vapor isotopic composition in Bermuda. Bermuda Island shape in dark grey and water
135 depth as color scale (Hijmans, 2015; NOAA, 2019); position of Tudor Hill Marine Atmospheric Observatory (white dot)
136 and wind sector to discriminate local transpired water vapor (red lines). Colored circles and triangle are the
137 sampling locations of available salinity and SST time series around the study area. The large-scale map on the left

138 shows the location of Bermuda (cross) in the northwest Atlantic Ocean and the main water vapor sources during the
139 study period. The highlighted sector includes 45% of accounted water vapor uptakes.

140

141 Due to its position and climatic conditions, the island of Bermuda is an ideal study site for
142 evaporation-related processes and their control on the d-excess signal because ocean evaporation
143 is the dominant source of the marine boundary layer vapor and there is low influence of
144 continental water vapor. Given that Bermuda is located in part of the source region for the
145 precipitation which is deposited in Greenland, this study is also relevant for ice core science
146 (Faber et al., 2020; Johnsen et al., 1989; H. Sodemann et al., 2008). Specifically, it poses new
147 questions about the information deduced from climate proxies in paleoclimate archives (e.g.
148 Jouzel et al., 2007; Steen-Larsen et al., 2011, Markle et al., 2018). Therefore, the sensitivity of
149 non-equilibrium fractionation factors to ocean composition and to SST variability and the impact
150 on the d-excess sensitivity to evaporative condition over the ocean are also discussed.

151 **2 Materials and Methods**

152 **2.1 Study site**

153 The study site is located in the south-western part of the Bermuda Main Island, at the Tudor Hill
154 Marine Atmospheric Observatory (THMAO) tower of Bermuda Institute of Ocean Sciences
155 (32.26° N 64.88° W). The THMAO tower faces the coast (distance ~ 30 m) and is 20.5 m high.
156 Considering the altitude of the tower base (~ 29 m AMSL), the top of the tower faces the ocean at
157 a height of ~ 50 m AMSL. The climatic conditions at Bermuda Island are characterized by humid
158 subtropical climate, strongly affected by the Gulf Stream. The study area is situated in the so-
159 called Bermuda-Azores High, a large subtropical center of high atmospheric pressure. The high-
160 pressure system is strong and centered near the Bermuda Islands during the summer and related
161 to the intensity of the Icelandic Low. Ocean evaporation around Bermuda Island is strong due to
162 its location in Gulf Stream area and by the influence of unsaturated air transported off the
163 American Continent, especially during the winter. ERA5 reanalysis data (Hersbach et al., 2020)
164 shows that the evaporation flux (E) in the study area exceeds the precipitation flux (P), as
165 expected ($P-E = -1.34$ mm day $^{-1}$). WaterSip moisture source diagnostic (Sodemann & Läderach,
166 2021) for the Jun-Dec 2013 calculated with $1^{\circ} \times 1^{\circ}$ 6h time step resolution ERA-Interim reanalysis
167 (Dee et al., 2011) revealed that 45% of lower tropospheric moisture originated in a $10^{\circ} \times 10^{\circ}$ area
168 around the study site (inset map in Figure 1).

169 **2.2 Meteorological and ocean observations**

170 Air temperature, relative humidity (T, RH, Campbell Scientific EE181-L125-PT), wind speed
171 and wind direction (WS, WD, R.M. Young CAT NO. 05103) were measured at the top inlet (50
172 m AMSL) of THMAO. The wind speed measured at 50 m ASL was corrected to 10 m AMSL
173 assuming a log-law wind profile and a roughness length of 0.2 mm (Stull, 1997). Sea Level
174 Pressure (SLP) and precipitation (P) were measured ~ 20 km northeast at the L. F. Wade
175 International Airport (TXKF) by the Bermuda Weather Service. Boundary Layer Height (BLH)
176 data was taken from ERA5 global reanalysis at $0.25^{\circ} \times 0.25^{\circ}$ and 1-hour temporal resolution.
177 BLH gridded data was linearly interpolated at the study site location.

178 **2.3 SST and Ocean water isotopic composition**

179 Salinity and SST observations are available from buoys inside the reef at 3h time resolution (Hog
180 Reef and Crescent Reef), at St. George Harbor at daily resolution and outside the reef at monthly

181 resolution for the Bermuda Atlantic Time-series Study (BIOS, 2021). Salinity and SST
182 measurement locations are reported in Figure 1. To minimize potential bias due to local SST
183 variations we chose the averaged Operational Sea Surface Temperature and Sea Ice Analysis
184 (OSTIA, UK MET OFFICE, 2005) data as representative for SST of the study site. High
185 correlation is observed between average SST measured inside the reef and OSTIA product (R
186 Pearson > 0.96) but better agreement, in terms of maximum absolute difference, was observed
187 between BATS and OSTIA data (1.08 °C) than for Crescent reef and OSTIA data (2.55 °C).

188 No measurements of ocean water isotopic composition near the study site are available for the
189 period of interest, but the temporal variability of the ocean isotopic composition in the study area
190 is assumed to be very low. Several sources have been evaluated for estimating the most
191 representative composition of ocean water around the study site: gridded dataset (LeGrande &
192 Schmidt, 2006), North Atlantic cruises published data (Benetti et al., 2014, 2017) as well as from
193 samples collected at the BATS site two years before this campaign (BIOS, 2021). The average
194 isotopic composition of the ocean in this study is assumed to be $\delta^{18}\text{O}_L = 1.09\text{‰}$ and $\delta\text{D}_L =$
195 7.25‰ , which is the average of the salinity to isotope conversion (Benetti et al., 2017) from
196 gridded dataset and BIOS data. Full details on ocean water isotopic composition are reported in
197 Supporting Info, Text S1.

198 **2.4 Water vapor isotopic composition and humidity observations**

199 Ambient air was sampled at THMAO tower at two different heights: 2.5 m and at 50 m AMSL.
200 Ambient air was continuously pumped from the two inlets to a manifold located at the tower
201 base that was connected to a Picarro L2120-i isotopic water vapor Cavity Ring-Down
202 Spectroscopy (CRDS) analyzer. Quick air transport was ensured through heated copper tubing
203 using a 10 L min^{-1} sampling pump. The sampling line was switched between the two inlets every
204 15 minutes and when one inlet was connected to the analyzer, the other inlet was flushed by a
205 secondary 5 l min^{-1} pump. This configuration ensured a continuous circulation of air inside the
206 tubing system, thus minimizing the lag and memory effect for the two inlets. The CRDS analyzer
207 recorded humidity and water isotopic composition at $\sim 0.56\text{ Hz}$ frequency. To reduce the memory
208 effect due to the switching between top and bottom inlet, the first 10 minutes of data after valve
209 switching was removed and the last 5 minutes was averaged. In this way, the 5 minutes average
210 is assumed to be representative of the isotopic composition during measurement for each level.
211 The inlet can be approximated to a first-order low pass filter with transfer function $H=1/(\tau+1)$,
212 where τ is the time the system's response need to reach 63% of the final value for a step change
213 from zero initial condition ($\tau(\delta^{18}\text{O}) = 212\text{ s}$, $\tau(\delta\text{D}) = 310\text{ s}$). We estimated that the magnitude of
214 signal attenuation is only -1.9 dB for $\delta^{18}\text{O}$ and -3.4 dB for δD and the phase difference between
215 $\delta^{18}\text{O}$ and δD signal is $<9^\circ$ with an averaging window of 0.5 hours. Therefore, the error
216 introduced by signal attenuation and phase difference between $\delta^{18}\text{O}$ and δD signal in the sensing
217 system is not significant at the time resolution used in this study.

218 The isotope readings of the water vapor analyzer were calibrated on the VSMOW-SLAP scale
219 (IAEA, 2009) using several laboratory standards at the beginning and towards the end of the
220 measurements. Drift-correction measurements were carried out on a sub-daily basis (every 6-12
221 hours) and several humidity-isotope response curves were performed during the study period to
222 correct for the humidity dependency of water vapor isotopic composition. Precision of water
223 vapor isotopic measurement are expected to be 0.14‰ for $\delta^{18}\text{O}$ and 1.1‰ for δD . The reader is
224 referred to a previous study conducted at THMAO for additional details on calibration protocol

225 (Steen-Larsen et al., 2014). Humidity observations of the CRDS analyzer (moist mixing ratio, w
226 [ppmv]) were calibrated against RH observations at the top inlet.

227 **2.5 Estimation of evaporation flux isotopic composition**

228 Isotopic water vapor observations acquired with CRDS analyzer represent the time-averaged
229 atmospheric moisture composition at a certain height above sea level. We used the Keeling Plot
230 (KP) gradient method between the two inlets to estimate the isotopic composition of the water
231 vapor flux (δ_E). In the KP method, δ_E is assumed to be equal to the intercept of the linear best-fit
232 model between the isotopic composition of water vapor ($\delta^{18}\text{O}$ or δD) and the inverse of humidity
233 ($1/w$) at the two different height levels (Keeling, 1958). Uncertainties for δ_E were calculated as a
234 function of instrument precision, sample size, and atmospheric conditions (Good et al., 2012).
235 However, in our case the number of observations for each time-step is equal to the degrees of
236 freedom required to calculate the uncertainty associated with the flux composition. Therefore,
237 observations were grouped on a daily basis and the error on flux composition was calculated when
238 more than two observations were available. It is important to note that the computation of flux
239 composition with KP method is valid only under the following assumptions:

- 240 1. The mixing process in the gradient measurement space is fully turbulent and does not
241 introduce any fractionation: turbulent diffusion is the same for all isotopologues.
- 242 2. Water vapor flux is constant with height: the mixing ratio and water vapor isotopic
243 composition vertical profiles is characterized by a monotonic trend.
- 244 3. Variability of water vapor isotopic signal is not significantly affected by advection during
245 the acquisition of water vapor profiles.
- 246 4. Isotopic composition of source water is constant in the time interval considered.

247 Therefore, water vapor observations were subset and filtered, to fulfill the above mentioned
248 assumptions, as further discussed in Section 3.2 and Section 5.1. Because of the sensitivity to
249 different fetch areas for the bottom and top inlets, water vapor isotopic composition at the bottom
250 inlet was corrected ($\delta^{18}\text{O}=+0.07\text{‰}$ and $\delta\text{D}=+0.75\text{‰}$) accounting for the SST difference between
251 open ocean SST and reef area SST, as further discussed in Section 5.2.

252 **2.6 Estimation of non-equilibrium fractionation factors**

253 The Craig Gordon (CG) model was used to calculate δ_E from the ocean surface (Craig & Gordon,
254 1965) following the notation introduced in (Merlivat & Jouzel, 1979), as reported in equation
255 (1):

$$256 \quad \delta_E = (1 - k) \frac{\alpha_{V/L}^{(1+\delta_L)-h(1+\delta_A)}}{(1-h)} - 1 \quad (1)$$

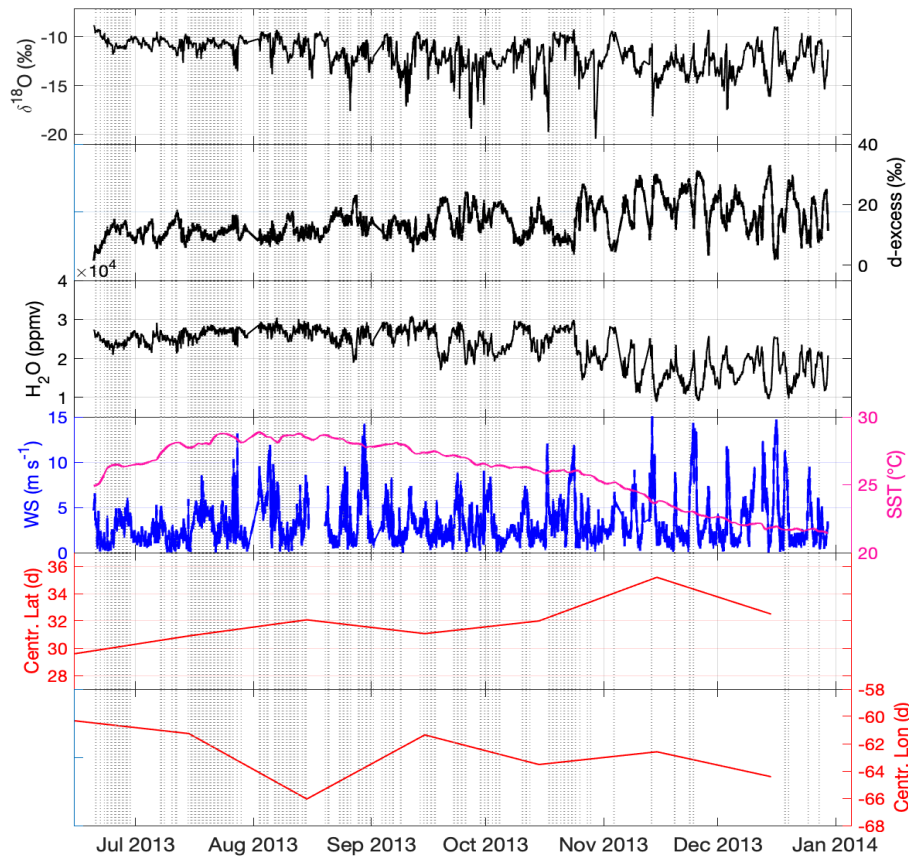
257 where $\alpha_{V/L}$ [<1] is the equilibrium fractionation factor between vapor and liquid (Horita &
258 Wesolowski, 1994), h [0-1] is the relative humidity of the free atmosphere relative to ocean
259 surface temperature, k is the non-equilibrium fractionation factor, δ_A is the isotopic composition
260 of atmospheric moisture, δ_L is the isotopic composition of the ocean water. The non-equilibrium
261 fractionation factor k is estimated from a direct comparison between observed (KP) and modeled
262 (CG) isotopic composition of the evaporation flux. For a given flux observation i , it is possible to
263 calculate m different values of the flux composition with CG model by varying the non-
264 equilibrium fractionation factors within a certain range. The best k values are then calculated by
265 error minimization between modeled and observed evaporation flux composition for each pair of

266 top and bottom inlet observations. To estimate the average values of k , the errors of the observed
 267 flux composition were used as the weights in the computation of the average. Populations of
 268 mean non-equilibrium fractionation factors k and 95% confidence interval of the mean were
 269 estimated with bootstrapping, repeating the above sequence for 10^4 times with random
 270 resampling. Additional details on how the non-equilibrium fractionation factors are calculated
 271 are reported in Supporting Info, Text S2 and Text S3.

272 3 Data description

273 3.1 Dataset

274 Time series of water vapor at top and bottom inlets were resampled using a common UTC time
 275 indexing with a resolution of 30 minutes through linear interpolation. Meteorological observations
 276 were also averaged and synchronized accordingly to CRDS observations. The water vapor time
 277 series used in this study includes 8793 datapoints, representative of 30-minutes averaged
 278 observations of water vapor isotopic composition at two height levels over the ocean surface. The
 279 complete dataset accounts for 95% coverage of the study period (Figure 2).



280
 281 **Figure 2:** Timeseries of water vapor isotopic composition and relevant meteorological parameters at study site.
 282 Water vapor isotopic composition and wind speed (WS) measured at top inlet height (50 m AMSL). SST data from
 283 OSTIA. Centroid of moisture source area (latitude weighted) estimated with WaterSip. Vertical lines represent
 284 selected observations for water vapor flux estimation.

285 Based on d-excess, the pattern of atmospheric water vapor composition can be divided in two
 286 main groups: a first group from summer to mid-autumn with gentle daily to weekly d-excess
 287 oscillations and a second group, from mid-autumn to early winter, with larger and more
 288 pronounced d-excess oscillations at weekly scale. The transition in the d-excess pattern follows
 289 the general decrease in humidity after late October. The temperatures decrease in autumn-winter
 290 is also highlighted by the influence of different moisture sources areas, with a general shift of
 291 atmospheric water vapor origin toward the north-west (from 30 °N to 35 °N and from 60° W to
 292 64° W, for latitude and longitude, respectively). The north-western shift in moisture sources
 293 areas highlighted here is linked to the increase in baroclinicity towards autumn and winter and to
 294 the more frequent passage of extratropical cyclones over the gulf stream (Aemisegger & Sjolte,
 295 2018).

296 3.2 Filtered dataset for flux estimation

297 To guarantee high data quality and for maximizing the validity of assumptions under KP
 298 (Section 2.5, points 1 - 4), several constraints were introduced to filter the dataset. The rationale
 299 behind those constraints is summarized for each variable in Table 1.

300 **Table 1:** List of variables and constraints adopted to filter the time series.
 301

Variable	Indexing	Range/Value	Rejected (cumulative)	Assumption #	Rationale
Time	Time	Daytime observations based on sunrise-sunset hour (LST) with 2 hours offset	71%	2,4	No influence of dew formation caused by night cooling.
WD	Wind sector inclusion	Western Sector 180°N – 340°N (i.e. excluding winds from inland)	85%	3,4	No influence of local evapotranspiration from vegetation
δD and $\delta^{18}O$	$ \delta D_{\text{Bottom}} - \delta D_{\text{Top}} $ $ \delta^{18}O_{\text{Bottom}} - \delta^{18}O_{\text{Top}} $	$> 1 \text{ ‰}$ $> 0.1 \text{ ‰}$	89%	2	Difference between Top/Bottom larger than instrumental precision (L2120-i)
w	$w_{\text{Bottom}} - w_{\text{Top}}$	$> 100 \text{ ppmv}^*$	89%	2	w decreases with height above ocean.
P	Time	No precipitation within the last two hours	90%	1,2,3,4	No vapor recycling from precipitation

302
 303 The column “rejected” reports the size of dataset that does not fulfill each filtering threshold. Assumption n# refers to
 304 the numbered list in Section 2.5. * This is a conservative estimate of instrumental precision not reported in the L2120-
 305 I datasheet.

306 By means of the quality control filtering criteria, the sample size is reduced from 8793 to 814 30-
 307 minutes averaged observations (~10% of available data). The variables that are most responsible
 308 for the exclusion of data points are daytime and the western wind sector constraints. Just those
 309 two filtering criteria accounts for approximately 85% of rejections. However, this strict filtering
 310 criteria was necessary because of the strong local evapotranspiration signal developing during
 311 the night and with wind blowing from inland. The remaining filtering criteria accounted for an
 312 additional 5% of rejections.

313 Most of the observations (~90%) of the filtered dataset were selected between 20th June and 23th
 314 October, as shown in Figure 2. From the perspective of data representativeness, the main features
 315 of the dataset after the filtering procedure are: (i) slightly changed mean and median values (for
 316 $\delta^{18}\text{O}$ and d-excess) and reduction of secondary modes in d-excess distribution; (ii) statistically
 317 significant change in regression parameters for d-excess vs RH with respect to SST (hereafter h);
 318 (iii) significant reduction of observations characterized by deeper PBL (PBLH > 1000 m, from
 319 17% to 4%); (iv) change of the wind speed distribution in terms of the mean (from 2.8 ms^{-1} to
 320 4.0 ms^{-1}). Therefore, the main consequences of data reduction are a larger impact of shallow
 321 atmospheric mixing, a smaller influence of large MBL development and lower frequency of low
 322 wind speed conditions. More details on the impact of data filtering on the distribution shape of
 323 variables of interest are reported in Supporting Info, Text S4.

324 4 Results

325 4.1 The isotopic composition of evaporation flux (δ_E) from the ocean surface

326 Descriptive statistics of the evaporation flux isotopic composition from the ocean surface and the
 327 water vapor isotopic composition observed at the top inlet during daytime are reported in Table 2.

328 **Table 2:** Descriptive statistics of evaporation flux and top inlet water vapor isotopic composition at the daily
 329 timescale.

	Mean (‰)	Median (‰)	IQR (‰)	σ_{δ_E} (‰)
Evaporation flux $\delta^{18}\text{O}$	-3.37	-4.48	-6.7 ; -0.04	1.17
Evaporation flux δD	-24.99	-33.48	-48.38 ; -1.60	7.33
Top inlet water vapor $\delta^{18}\text{O}$	-11.30	-10.97	-12.10 ; -10.51	-
Top inlet water vapor δD	-78.13	-76.14	-83.15 ; -73.10	-

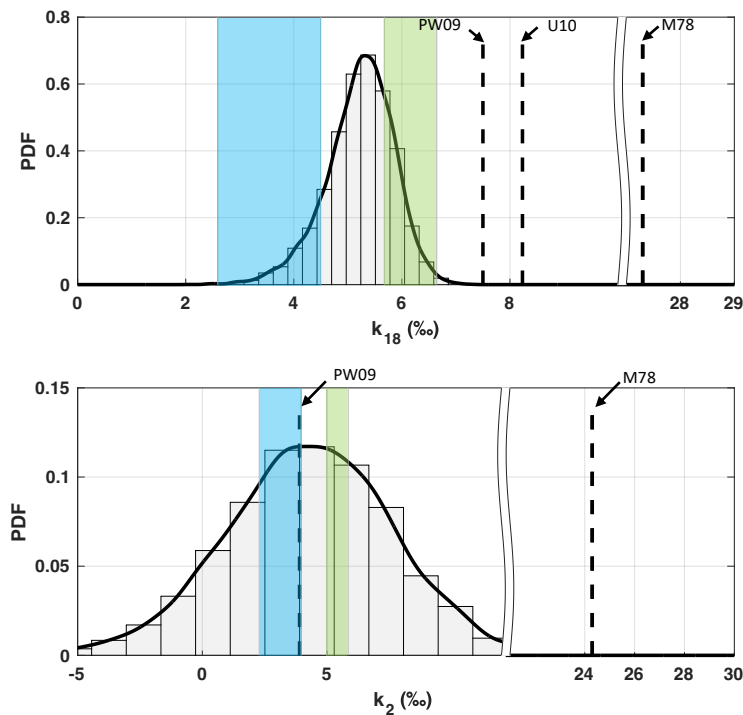
330 On average, the number of data points available for KP calculation is 20 per day and the
 331 coefficients of determination for both $\delta^{18}\text{O}$ and δD regression lines are high ($R^2 = 0.78$, on
 332 average). For comparison, the Flux Gradient method (FG, Lee et al., 2007) was also used to
 333 compute the isotopic composition of evaporation flux, obtaining nearly identical results but
 334 different uncertainties, especially for δD ($\sigma_{\delta_E} = 0.59\text{‰}$ and 51‰ for $\delta^{18}\text{O}$ and δD , respectively).
 335 The high similarity between the FG and KP methods is consistent with other studies (Good et al.,
 336 2012; Hu et al., 2021).

337 As expected, the isotopic composition of the flux is enriched with respect to the atmospheric
 338 water vapor composition. The mean δD of the evaporation flux is in between recent estimates of

339 the global mean HDO cycle (-37.6‰ following Good et al., 2015) and estimates made in past
 340 studies (-22‰ following e.g. Gat, 1996). No evident trend was observed for daily δ_E during the
 341 study period, for both $\delta^{18}\text{O}$ and δD .

342 4.2 Non-equilibrium fractionation factor distributions estimated with flux observations

343 Non-equilibrium fractionation factors are expressed hereafter in term of k_{18} (for $\delta^{18}\text{O}$) and k_2 (for
 344 δD) to allow a direct comparison with the parametrization of (Merlivat & Jouzel, 1979). Applying
 345 the bootstrapping method with 10^4 repetitions in the filtered dataset we obtained mean \pm 1 std. dev.
 346 $k_{18} = 5.21 \pm 0.64\text{‰}$ and $k_2 = 4.32 \pm 3.41\text{‰}$, as show in Figure 3.



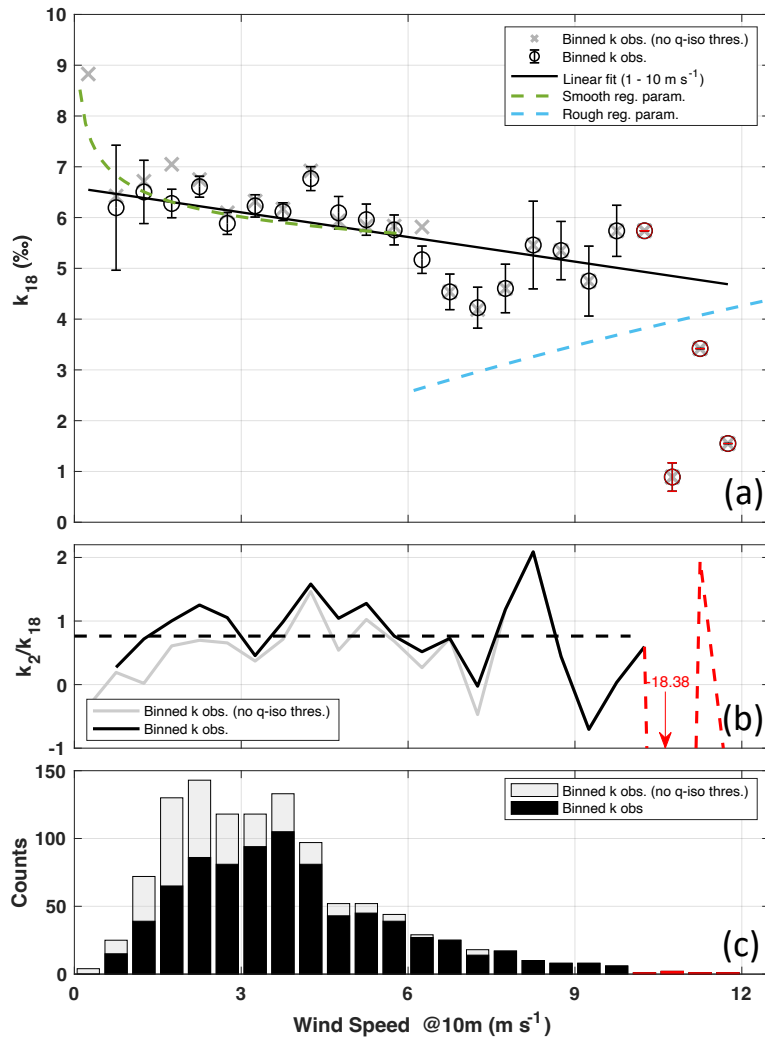
347
 348 **Figure 3:** Non-equilibrium fractionation factors estimated from flux observations (KP method). Continuous kernel
 349 density function was estimated with bandwidths 0.1‰ and 0.6‰ for k_{18} and k_2 , respectively. Shaded area represents
 350 the k intervals predicted for smooth (green, 10-m wind speed range 1-6 m s^{-1}) and rough (cyan, 10-m wind speed
 351 range 6-13 m s^{-1}) regimes following Merlivat and Jouzel (1979). For reference, diffusivity ratios M78 (Merlivat,
 352 1978) and non-equilibrium fractionation factors PW09 (Pfahl & Wemli, 2009) and U10 (Uemura et al., 2010) are
 353 reported as vertical dashed lines.

354 The obtained k PDFs are in the range predicted by the parametrization proposed in (Merlivat &
 355 Jouzel, 1979). For k_{18} , the distribution of the mean values falls in the middle of the
 356 parametrizations for the smooth and rough wind speed regimes. A similar result was obtained for
 357 mean k_2 , which PDF is however characterized by significantly larger spread. Consistent with
 358 previous works, non-equilibrium fractionation factors are on average $\sim 0.20 - 0.25$ times the value
 359 expected for a purely diffusivity-driven evaporation process (Merlivat, 1978). For reference, the
 360 k values estimated in other studies are also reported in Figure 3 (Pfahl & Wemli, 2009; Uemura
 361 et al., 2010). Note that the k_{18} values estimated in this study are 2-3 ‰ smaller than previous
 362 studies and more consistent with the parametrization of k_{18} proposed in (Merlivat & Jouzel,

1979). On average the ratio k_2/k_{18} is equal to 0.83, similar to (Merlivat & Jouzel, 1979) and (Luz et al., 2009), who also demonstrated that air temperature between 20°C and 40°C has a minimal effect on this ratio (the sensitivity is $\sim 5 \times 10^{-3} \text{ } ^\circ\text{C}^{-1}$).

4.3 Observed relationship between non-equilibrium fractionation factors and 10-m wind speed

The filtered dataset was binned in 10-m wind speed classes with bin size 0.5 m s^{-1} to estimate the relationship between $k_{2,18}$ and wind speed. For each wind speed class, the non-equilibrium fractionation factors were calculated using the KP method at 30 min time step. Afterwards, mean and standard error of $k_{2,18}$ were calculated for each wind speed bin center. Mean k_{18} values obtained in such way are reported as a function of 10-m wind speed in Figure 4.a.



374 **Figure 4:** Observed relationship between k_{18} and 10-m wind speed. (a) mean \pm standard error of k_{18} estimated for
 375 each wind speed class. Green and cyan lines show the parametrization of k_{18} for smooth and rough wind regimes,
 376 respectively (Merlivat & Jouzel, 1979). Solid black line represents a linear fit ($R^2=0.52$) in the wind speed interval
 377 $0.5 - 10 \text{ m s}^{-1}$ (fit equation reported in text). (b) k_2/k_{18} ratio for each wind speed class. Dashed black line is the
 378 average ratio (0.8). (c) Number of observations for each bin. In all panels: black lines, black symbols and black bars
 379 for filtered dataset; gray lines, gray symbols and gray bars for filtered dataset with no isotope and humidity
 380

381 thresholds implemented: red line, red symbols and red bars highlight wind speed classes with number of observation
 382 ≤ 2 .

383 In the wind speed range $[0.5 - 10] \text{ m s}^{-1}$ the negative correlation between k_{18} and wind speed is
 384 high and statistically significant ($r=-0.72$, $p\text{-value}=1 \times 10^{-3}$). The parametrization proposed in
 385 (Merlivat & Jouzel, 1979) predicts with good accuracy the range of observed k_{18} variability
 386 between 0.5 and 6 m s^{-1} , with an average absolute difference of 0.1% . Most importantly, the
 387 differences between parametrized and observed k_{18} values are normally distributed around zero
 388 (Kolmogorov-Smirnov and Shapiro-Wilk p -values equals to 0.13 and 0.34 , respectively) and the
 389 errors can therefore be attributed to random noise in the measurement. On the other hand, observed
 390 k_{18} are 2% larger than modeled k_{18} for rough regime parametrization between 6 and 10 m s^{-1} .
 391 Moreover, the theoretical wide discontinuity between smooth and rough regime expected at $\sim 6 \text{ m}$
 392 s^{-1} can not be resolved. A decrease of k_{18} in the $7 \pm 1 \text{ m s}^{-1}$ wind speed region is visible but k_{18}
 393 observations quickly aligns to the main decreasing trend. The observed k_{18} values are on average
 394 66% higher than the ones calculated with the rough regime parametrization. In other words, this
 395 study: (i) does not provide sufficient experimental evidence that there are two different regimes in
 396 the wind dependency of k_{18} and (ii) suggests that a continuous decrease of k_{18} as a function of wind
 397 speed is more likely in the interval $[0.5 - 10] \text{ m s}^{-1}$. Such decrease can be approximated by the
 398 following simplified equation:

$$399$$

$$400 \quad k_{18} = (-0.16 \pm 0.04) * \text{WS} + (6.6 \pm 0.3) \text{‰} \quad (2)$$

401 where WS is the 10-m wind speed in m s^{-1} . Equation (2) highlights that in the wind speed range
 402 $[0.5 - 10] \text{ m s}^{-1}$ the sensitivity of k_{18} to wind speed is only $-0.16 \pm 0.04 \text{‰ m}^{-1}\text{s}$. Data filtering
 403 prevents to calculate k_{18} at lower wind speed values, mainly because of the threshold on humidity
 404 and isotopic composition differences between the two inlets. When such thresholds are removed,
 405 the number of observations increases on the left side of the wind speed distribution (Figure 4.c),
 406 with a $\sim 5\%$ increase of the sample size. Despite that enables to include steeper gradient
 407 observations, a larger uncertainty is estimated for the lowest wind speed bin ($\text{SE}=1.7\%$, not
 408 shown). The impact of the presence/absence of humidity and isotopic composition difference
 409 thresholds between the two inlets is minimal in the k_{18} wind speed relationship. Indeed, the average
 410 absolute difference of k_{18} with/without those thresholds is only 0.1% in the $[0.5 - 10] \text{ m s}^{-1}$ wind
 411 speed range, with a minimal increase of the slope of 0.04% m^{-1}s . Unfortunately, the limited
 412 number of datapoints above 10 m s^{-1} does not allow any other speculation on the dependency of
 413 k_{18} to higher wind speed. It is possible, however, that other processes such as sea spray contribution
 414 might start to become important in the net evaporation flux above a certain wind speed threshold
 415 (Andreas et al., 1995; Veron, 2015). Therefore, equation (2) must be considered valid only in the
 416 $[0.5 - 10] \text{ m s}^{-1}$ wind speed range.

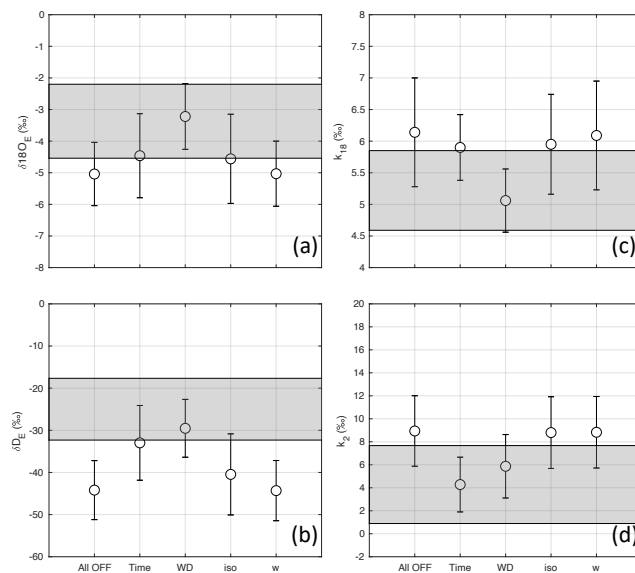
417
 418
 419 Continuing with k_2 , observations are scattered and very noisy on the k_2 vs wind speed plane (data
 420 reported in Supporting Info, Figure S5), as a result of δD less influenced by non-equilibrium
 421 fractionation than $\delta^{18}\text{O}$. The correlation between k_2 and wind speed is low and not significant
 422 within the $[0.5 - 10] \text{ m s}^{-1}$ wind speed range ($r=-0.34$, $p\text{-value}=0.15$). Observations are not in
 423 agreement with (Merlivat & Jouzel, 1979) parametrization, nor for the smooth nor for the rough
 424 regime, with an average absolute difference of 1.4% from the model. The noise in k_2 observations
 425 drastically affects the variability of the k_2/k_{18} ratio, which shows an average value of 0.8 and a

426 standard error of 0.1 (Figure 4.b). It is worth noting that the k_2/k_{18} ratio is not correlated with 10-
 427 m wind speed.
 428

429 5. Discussion

430 5.1. Method sensitivity to filtering criteria

431 The KP method is based on assumptions that might not be considered always valid in a dynamic
 432 oceanic environment. Even on an island in the middle of the ocean, local evaporation sources,
 433 such as vegetation and wind direction variability, can affect the validity of a simplified binary
 434 mixing model with ocean and free atmosphere as the only end members. The strict filtering
 435 criteria used in this study to estimate the isotopic composition of the evaporation flux and the
 436 non-equilibrium fractionation factors tries to select the data for maximizing the validity of the
 437 assumptions behind an ideal binary mixing model. This strict filtering, however, reduced the
 438 original dataset size significantly, as mentioned before. Here we discuss how each filtering
 439 criteria affects the results shown in Section 4.1 - 4.3, removing only data that can be affected by
 440 moisture input from precipitation events (Figure 5).



441
 442 **Figure 5:** Sensitivity of the method for estimating δ_E and k values to filtering criteria. Following Table 1: only
 443 precipitation filter (All off, $n = 6834$), time + precipitation filter (Time, $n = 2016$), wind sector + precipitation (WD,
 444 $n = 3143$), isotopic gradient + precipitation (iso, $n = 3883$), humidity gradient+ precipitation (w, $n = 6484$). **(a)** and
 445 **(b)** sensitivity of isotopic composition of evaporation flux (δ_E) for $\delta^{18}O$ and δD , respectively. **(c)** and **(d)** sensitivity
 446 of non-equilibrium fractionation factors for k_{18} and k_2 , respectively. For all panels, gray shaded areas represent
 447 ± 1 std. deviation when enabling all filtering steps.

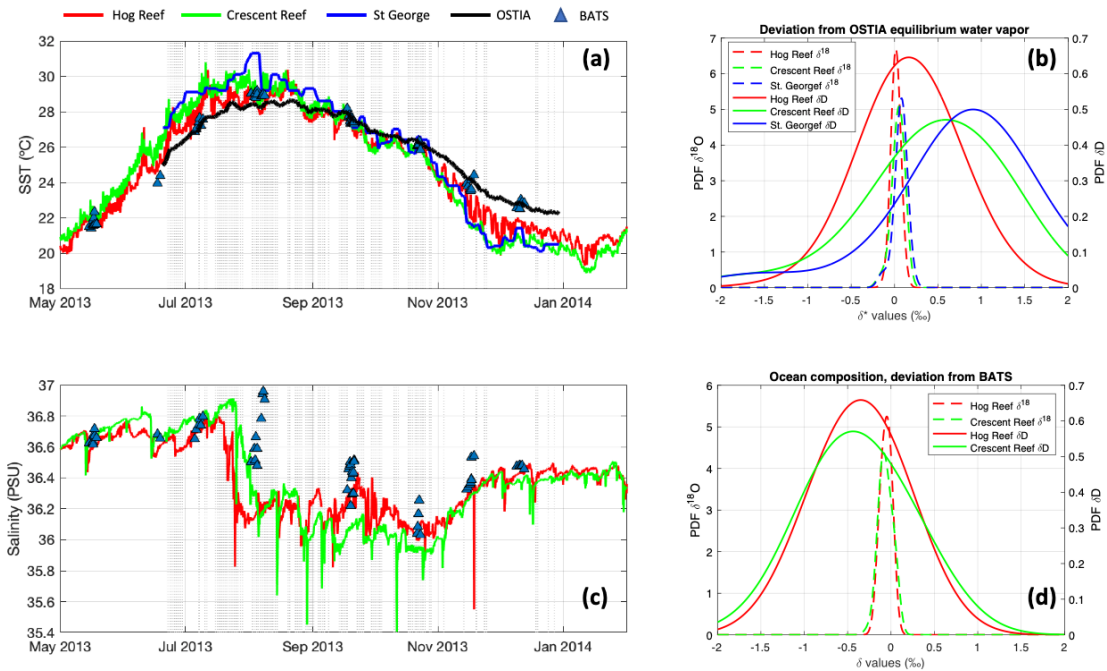
448 When all the filters are switched off, the isotopic composition of the evaporation flux decreases
 449 significantly and the mean δ_E values seem to not reflect evaporation from the ocean (Gat, 1996;
 450 Good et al., 2015; Craig & Gordon, 1965), as shown in Figure 5.a and b. Both daytime and
 451 western wind sector filters contribute enriching the isotopic composition of the flux. However,
 452 westward wind direction has the largest impact on $\delta^{18}O$ flux while daytime and westward wind

453 direction filtering contributes likewise on δD flux. This different impact for $\delta^{18}O$ and δD fluxes
454 highlights the different sensitivity of the method to environmental changes in daytime-nighttime
455 temperatures (larger effect on δD , minimal on $\delta^{18}O$) and on water vapor sources (ocean source vs
456 local evapotranspiration, similar effect for both δD and $\delta^{18}O$). The lower night temperatures,
457 coupled to the poor ventilation due to low wind speed during the night (data not shown) increase
458 RH substantially and enhance the contribution of local evapotranspiration. The k values show the
459 mirror image of the evaporation flux composition. Indeed, wind direction filtering contributes the
460 most on decreasing k_{18} value while time and wind direction contributes nearly equally for
461 decreasing k_2 . The steepness of isotopic and humidity gradients have only a marginal impact on
462 the average flux composition and k estimation.

463 **5.2 Impact of ocean surface composition and SST on k estimation**

464 Top and bottom inlets are sensitive to different fetch areas because of the wide height gap
465 between the two inlets at THMAO (~48 m). An analysis of the fetch areas performed with the
466 flux footprint prediction model (Kljun et al., 2015) suggested that 90% of the fetch area for the
467 bottom inlet is within 100 m while for top inlet is within 2800 m. Bermuda Island is
468 characterized by shallow waters close to the coast. Therefore, it is possible that local circulation
469 of ocean water within the reef can have an impact on SST variability and on surface water
470 isotopic composition. Continuous measurement of SST and ocean isotopic composition covering
471 the whole study area are not available. However, it is possible to infer the SST and salinity
472 variability (as a proxy of evaporation) from buoys and BATS data, as shown in Figure 6.a and
473 Figure 6.b. SST variability can be used to estimate the equilibrium water vapor variability in the

474 study area (Figure 6.c) while the variability of salinity can be used to estimate the variability of
 475 ocean composition (Figure 6.d).



476
 477 **Figure 6:** SST and salinity inhomogeneity of ocean waters around the study site. (a) Time series of SST in different
 478 points of the study area, see Figure 1 for reference of sampling sites. Vertical lines represent selected observations
 479 for flux estimation. (b) PDFs of [Equilibrium vapor (SST reef) – Equilibrium vapor (SST OSTIA)], where SST reef
 480 is the SST measured in different points within the reef area. (c) Similar to (a) but for salinity. (d) PDFs of [Ocean
 481 Composition (S reef) – Ocean Composition (S BATS)], where S reef is the salinity measured at different points
 482 within the reef area and S BATS is salinity measured at the BATS site. Conversion of salinity to isotopic
 483 composition following Benetti et al. (2017).

484 It is reasonable to assume that OSTIA SST is more representative of the isotopic composition of
 485 equilibrium water vapor for the top inlet while the SST measured within the reef is more
 486 representative for the bottom inlet. Therefore, it is possible to correct the water vapor isotopic
 487 composition at the bottom inlet by adding the mean deviation of St. George equilibrium SST
 488 from OSTIA, that is +0.07‰ and +0.75‰ for $\delta^{18}O$ and δD , respectively (i.e. the mean of blue
 489 PSD in Figure 6.b). As anticipated in Section 2.5, we used this correction to calculate the
 490 isotopic composition of evaporation fluxes shown in this study. Similarly, the ocean composition
 491 within the reef might be more representative of evaporating water within the reef, hence, an
 492 approximate offset can be added to the isotopic composition of the ocean equals to -0.06‰ and -
 493 0.38‰ for $\delta^{18}O$ and δD , respectively (i.e. the mean of the green PSD in Figure 6.d). Here we
 494 discuss how large is the impact of SST and ocean composition variability on estimation of the k
 495 values and their relationship with wind speed.

496 **Table 3:** Impact of SST and Ocean composition variability on $k_{2,18}$ and k_{18} vs wind speed parameters estimation.
 497 Uncertainties are: 0.6‰, 3.5‰, 0.04 and 0.3 for k_{18} , k_2 , slope and intercept, respectively. Deviation estimated from k
 498 values obtained without any correction.

Correction	Cause	k_{18} (‰)	Dev. (‰)	k_2 (‰)	Dev. (‰)	k_2/k_{18}	Slope (m^{-1} s)	Interc. (‰)
------------	-------	-----------------	-------------	--------------	-------------	--------------	------------------------	----------------

No correction	-	6.0	-	12.74	-	2.11	-0.20	7.93
Salinity correction	Different isotopic composition of surface water in fetch area	5.8	-4	11.37	-11	1.96	-0.21	7.72
SST correction	SST inhomogeneity in fetch area	5.2	-14	4.32	-66	0.83	-0.16	6.59
Salinity + SST corrections	SST and surface composition inhomogeneity	5.0	-18	2.81	-78	0.57	-0.17	6.37

499 As shown in Table 3, the inhomogeneity of ocean composition can introduce a bias in k_{18} and k_2
500 in the order of 0.3‰ and 1.3‰, respectively. These biases, are smaller than the uncertainties of
501 k_{18} and k_2 . On the other hand, SST inhomogeneity in the study area can introduce a 0.8‰ and
502 8‰ bias in k_{18} and k_2 estimation. When the SST correction is implemented, the k_{18} bias is still
503 comparable to k_{18} uncertainty while k_2 differs significantly when the offset is introduced (66%
504 absolute deviation). Therefore, SST has a larger impact on δD than on $\delta^{18}O$ and the impact of
505 ocean composition inhomogeneity in the study area is lower than the impact of SST in the
506 estimation of k_{18} and k_2 . It is worth to be noted that SST correction and Salinity + SST
507 corrections lower the k_2/k_{18} ratio below unity (0.83 and 0.57), thus giving a physical meaning to
508 the observation (e.g. see Table 2 in Horita et al., 2008 and reference therein). However, when
509 both Salinity and SST corrections are implemented, k_2 resulted too low and not consistent, e.g.
510 with recent water vapor observations in the Atlantic Ocean (Bonne et al., 2019). Finally, both
511 corrections do not affect significantly the observed correlation between k_{18} and wind speed. The
512 main effect of those corrections on k_{18} and k_2 is indeed to change the location of their PDFs
513 without changing the shape of the PDF. This means that the effect introduced by the correction is
514 translated into changing the intercept of the best fit line of Figure 4.a but keeping mostly
515 unchanged its slope. The observed negative correlation between k_{18} and wind speed is then
516 consistent, regardless the correction implemented.

517 **5.3 Suggested k values**

518 Given that k_{18} observations are less sensitive k_2 to spatial differences of SST, we suggest using
519 the mean value of $k_{18}=5.2‰$ and $k_2=4.3‰$. Indeed, these k values are estimated using all the
520 observations that maximized the validity of KP method assumptions and then should be
521 representative of the mean. In General Circulation Models, k_{18} can be calculated with the
522 observed linear relationship estimated with 10-m wind speed shown in equation (3) and k_2 can be
523 estimated by the average observed ratio of $k_2/k_{18}=0.83$. These values are valid for wind speed
524 between 0.5 and 10 m s⁻¹.

525 **5.4 D-excess sensitivity to evaporative conditions: need for further studies**

526 Assuming that water vapor d-excess signal is only modulated by local evaporation, the suggested
527 non-equilibrium fractionation factors of this study can be used to predict water vapor d-excess
528 using h (RH relative to SST) and the *Closure Assumption* (CA) (Bonne et al., 2019; Merlivat &
529 Jouzel, 1979; Pfahl & Wernli, 2009). However, there is a significant difference between the
530 regression parameters of the “d-excess vs h” line for CA and the observations in Bermuda (d-

531 excess = $-36.1 \cdot h + 35\%$ for CA, d-excess = $-46.2 \cdot h + 46\%$ for observations see Figure S3 in
532 Supporting Information). In general, the mean absolute difference between d-excess estimated
533 with CA and observed d-excess is 3.7‰. This discrepancy highlights how d-excess variability in
534 the MBL can be affected by additional processes than humidity deficit. Atmospheric mixing
535 between the boundary layer and the free atmosphere can be one those processes, changing the
536 free atmosphere end member isotopic composition and, at the same time, modulating h in the
537 MBL (Benetti et al., 2018; Risi et al., 2019). Following this idea, a simple regression model
538 based on observed d-excess, CA and Planetary Boundary Layer height is able to reproduce 82%
539 of the d-excess signal variability, showing that the 55% of variability can be attributed to h
540 variability and 22% to Planetary Boundary Layer height variability. Despite the validity of CA
541 and d-excess signal representativity in ocean water vapor is out of the scope of this study, we
542 expect this study to highlight the needs of more research effort to determine the processes
543 driving d-excess signal in the MBL at the daily – subdaily scale.

544 **6 Conclusions**

545 Profile observations of water vapor isotopic composition near the ocean surface can be used to
546 quantify the impact of non-equilibrium effects during natural evaporation in oceanic conditions.
547 In this study we provided a unique dataset of water vapor isotope observations collected at two
548 different heights on a meteorological tower in Bermuda Islands, North Atlantic Ocean. Using a
549 gradient-diffusion method we have extrapolated non-equilibrium fractionation factors
550 distributions for $^{18}\text{O}/^{16}\text{O}$ and $^2\text{H}/\text{H}$ during local evaporation and their relationship with wind
551 speed. A strict data filtering approach was used to maximize the validity of the assumptions
552 behind the gradient-diffusion method. The main downside of this approach is a consistent
553 reduction of the sample size but at the same time ensured a conservative approach for the
554 estimation of non-equilibrium fractionation factors. Observed non-equilibrium fractionation
555 factor for $^{18}\text{O}/^{16}\text{O}$ are in good agreement with smooth wind speed parametrization (mean ± 1
556 std.dev $k_{18} = 5.2 \pm 0.6\%$). The correlation between k_{18} and 10-m wind speed is statistically
557 significant, with a sensitivity in the order of -0.16 to $-0.20 \text{ m}^{-1} \text{ s}$. Such low sensitivity would be
558 nearly impossible to resolve by conventional measurements of water vapor d-excess at a single
559 height above the ocean surface. However, the observed relationship between k_{18} and wind speed
560 does not provide indication for the presence of a discontinuity between a smooth and rough
561 surface under different wind regimes. We note that the original smooth-rough regime wind speed
562 parametrization is based on the results of a single experiments at 7 m s^{-1} in Merlivat and Coantic
563 (1975), which actually do not fit the evaporation model of Brutsaert. A monotonic decrease of
564 k_{18} as function of wind speed is more likely for wind speeds up to $9 - 10 \text{ m s}^{-1}$. To this end, the
565 rough regime parametrization of k_{18} underestimates the observed fractionation factor by 66%.
566 Mean non-equilibrium fractionation factor for $^2\text{H}/\text{H}$ showed to be in the range expected by wind
567 speed parametrization (mean ± 1 std.dev $k_2 = 4.3 \pm 3.4\%$), but a larger degree of uncertainty is
568 reported for the determination of k_2 relationship with wind speed. We showed that the spatial
569 inhomogeneity of SST and ocean composition around the study site have a considerable impact
570 for the estimation of k_2 . On the other hand, estimation of k_{18} resulted to be consistent regardless
571 of the strict data filtering and of the spatial variability of SST and ocean composition. We
572 showed in addition that using the observed non-equilibrium fractionation factors with RH
573 measurements and information of Planetary Boundary Layer height allow us to explain 82% of
574 the water vapor d-excess variability in Bermuda. This poses the usefulness of new research effort

575 in understanding the physical controls of water vapor d-excess in the marine boundary layer at
576 daily – subdaily temporal resolution.

577 **Acknowledgments**

578 The work was supported by the Danish Council for Independent Research – Natural Sciences
579 grant number 10-092850 and the Carlsberg Foundation, and the AXA Research Fund. The Tudor
580 Hill Marine Atmospheric Observatory in Bermuda is supported by NSF award OCE1829686.
581 We acknowledge an infrastructure grant (nr. 10/0244) from the Icelandic Research Council
582 (Rannis), that partly covered the cost of the Picarro facilities in Bermuda. HCSL and DZ
583 acknowledges funding from the European Union’s Horizon 2020 research and innovation
584 programme under grant agreement no. 821868. H.S. acknowledges support by the Norwegian
585 Research Council (Project SNOWPACE, grant no. 262710) and by the European Research
586 Council (Consolidator Grant ISLAS, project no. 773245). SW acknowledges funding from the
587 European Research Council (ERC) under the European Union’s Horizon 2020 research and
588 innovation program: Starting Grant-SNOWISO (grant agreement 759526).
589

590 **Open Research**

591 The water vapor and meteorological time series used for calculating the non-equilibrium
592 fractionation factors in the study will be uploaded on Pangea, DOI to be minted with CC BY
593 4.0. Code for data analysis and for reproducing plots in the article is available at corresponding
594 author repository: <https://github.com/danielez83/Bermuda-NEFF>
595

596 **References**

- 597 Aemisegger, F., & Sjolte, J. (2018). A climatology of strong large-scale ocean evaporation
598 events. Part II: Relevance for the deuterium excess signature of the evaporation flux.
599 *Journal of Climate*, 31(18), 7313–7336. <https://doi.org/10.1175/JCLI-D-17-0592.1>
- 600 Andreas, E. L., Edson, J. B., Monahan, E. C., Rouault, M. P., & Smith, S. D. (1995). The spray
601 contribution to net evaporation from the sea: A review of recent progress. *Boundary-Layer*
602 *Meteorology*, 72(1–2), 3–52. <https://doi.org/10.1007/BF00712389>
- 603 Benetti, M., Lacour, J. L., Sveinbjörnsdóttir, A. E., Aloisi, G., Reverdin, G., Risi, C., et al.
604 (2018). A Framework to Study Mixing Processes in the Marine Boundary Layer Using
605 Water Vapor Isotope Measurements. *Geophysical Research Letters*, 45(5), 2524–2532.
606 <https://doi.org/10.1002/2018GL077167>
- 607 Benetti, Marion, Reverdin, G., Pierre, C., Merlivat, L., Risi, C., Steen-larsen, H. C., & Vimeux,
608 F. (2014). Deuterium excess in marine water vapor: Dependency on relative humidity and
609 surface wind speed during evaporation, 584–593.
610 <https://doi.org/10.1002/2013JD020535>. Received
- 611 Benetti, Marion, Reverdin, G., Aloisi, G., & Sveinbjörnsdóttir, Á. (2017). Stable isotopes in
612 surface waters of the Atlantic Ocean: Indicators of ocean-atmosphere water fluxes and
613 oceanic mixing processes. *Journal of Geophysical Research: Oceans*, 122(6), 4723–4742.
- 614 BIOS. (2021). Bermuda Atlantic Time-series Study (BATS).
- 615 Bonne, J. L., Behrens, M., Meyer, H., Kipfstuhl, S., Rabe, B., Schönicker, L., et al. (2019).
616 Resolving the controls of water vapour isotopes in the Atlantic sector. *Nature*
617 *Communications*, 10(1), 1–10. <https://doi.org/10.1038/s41467-019-09242-6>

- 618 Ciais, P., & Jouzel, J. (1994). Deuterium and oxygen 18 in precipitation: isotopic model,
619 including mixed cloud processes. *Journal of Geophysical Research*, 99(D8).
620 <https://doi.org/10.1029/94jd00412>
- 621 Craig, H. (1961). Isotopic variations in meteoric waters. *Science*, 133(3465), 1702–1703.
- 622 Dansgaard, W. (1964). Stable isotopes in precipitation. *Tellus*, 16(4), 436–468.
623 <https://doi.org/10.3402/tellusa.v16i4.8993>
- 624 Dee, D. P., Uppala, S. M., Simmons, A. J., Berrisford, P., Poli, P., Kobayashi, S., et al. (2011).
625 The ERA-Interim reanalysis: Configuration and performance of the data assimilation
626 system. *Quarterly Journal of the Royal Meteorological Society*, 137(656), 553–597.
627 <https://doi.org/10.1002/qj.828>
- 628 Faber, A.-K., Steen-Larsen, H. C., & Sodemann, H. (2020). Revisiting the origin of Greenland
629 moisture sources: Regional differences, seasonality and land/ocean sources. In *AGU Fall*
630 *Meeting Abstracts* (Vol. 2020, pp. C033--06).
- 631 Galewsky, J., Steen-Larsen, H. C., Field, R. D., Worden, J., Risi, C., & Schneider, M. (2016).
632 Stable isotopes in atmospheric water vapor and applications to the hydrologic cycle.
633 *Reviews of Geophysics*, 54(4), 809–865. <https://doi.org/10.1002/2015RG000512>
- 634 Galewsky, J., Jensen, M. P., & Delp, J. (2022). Marine Boundary Layer Decoupling and the
635 Stable Isotopic Composition of Water Vapor. *Journal of Geophysical Research:*
636 *Atmospheres*, 127(3), 1–14. <https://doi.org/10.1029/2021jd035470>
- 637 Gat, J. R. (1996). Oxygen and Hydrogen Isotopes in the Hydrologic Cycle. *Annual Review of*
638 *Earth and Planetary Sciences*, 24(1), 225–262.
639 <https://doi.org/10.1146/annurev.earth.24.1.225>
- 640 Gat, J. R., Klein, B., Kushnir, Y., Roether, W., Wernli, H., Yam, R., & Shemesh, A. (2003).
641 Isotope composition of air moisture over the Mediterranean Sea: An index of the air-sea
642 interaction pattern. *Tellus, Series B: Chemical and Physical Meteorology*, 55(5), 953–965.
643 <https://doi.org/10.1034/j.1600-0889.2003.00081.x>
- 644 Gonfiantini, R., Wassenaar, L. I., & Araguas-Araguas, L. J. (2020). Stable isotope fractionations
645 in the evaporation of water: The wind effect. *Hydrological Processes*, 34(16), 3596–3607.
646 <https://doi.org/10.1002/hyp.13804>
- 647 Good, S. P., Soderberg, K., Wang, L., & Caylor, K. K. (2012). Uncertainties in the assessment of
648 the isotopic composition of surface fluxes: A direct comparison of techniques using laser-
649 based water vapor isotope analyzers. *Journal of Geophysical Research Atmospheres*,
650 117(15), 1–22. <https://doi.org/10.1029/2011JD017168>
- 651 Good, S. P., Noone, D., Kurita, N., Benetti, M., & Bowen, G. J. (2015). D/H isotope ratios in the
652 global hydrologic cycle. *Geophysical Research Letters*, 42(12), 5042–5050.
653 <https://doi.org/10.1002/2015GL064117>
- 654 Griffis, T. J., Wood, J. D., Baker, J. M., Lee, X., Xiao, K., Chen, Z., et al. (2016). Investigating
655 the source, transport, and isotope composition of water vapor in the planetary boundary
656 layer. *Atmospheric Chemistry and Physics*, 16(8), 5139–5157. <https://doi.org/10.5194/acp-16-5139-2016>
- 657
- 658 H Craig, & Gordon, L. I. (1965). *Stable Isotopes in Oceanographic Studies and*
659 *paleotemperatures*.
- 660 Held, I. M., & Soden, B. J. (2000). Water Vapor Feedback and Global Warming. *Annual Review*
661 *of Energy and the Environment*, 25, 441–475.
- 662 Hersbach, H., Bell, B., Berrisford, P., Hirahara, S., Horányi, A., Muñoz-Sabater, J., et al. (2020).
663 The ERA5 global reanalysis. *Quarterly Journal of the Royal Meteorological Society*,

- 664 146(730), 1999–2049. <https://doi.org/10.1002/qj.3803>
- 665 Hijmans, R. J. (2015). Boundary, Bermuda, 2015. Retrieved from
666 <https://maps.princeton.edu/catalog/stanford-nw036zp7611>
- 667 Horita, J., & Wesolowski, D. J. (1994). Liquid-vapor fractionation of oxygen and hydrogen
668 isotopes of water from the freezing to the critical temperature. *Geochimica et*
669 *Cosmochimica Acta*, 58(16), 3425–3437. Retrieved from
670 <papers2://publication/uuid/F9BCD32F-8569-4ACF-81AF-08518BF40A32>
- 671 Horita, J., Rozanski, K., & Cohen, S. (2008). Isotope effects in the evaporation of water: A status
672 report of the Craig-Gordon model. *Isotopes in Environmental and Health Studies*, 44(1),
673 23–49. <https://doi.org/10.1080/10256010801887174>
- 674 Hu, Y., Xiao, W., Wei, Z., Welp, L. R., Wen, X., & Lee, X. (2021). Determining the Isotopic
675 Composition of Surface Water Vapor Flux From High-Frequency Observations Using Flux-
676 Gradient and Keeling Plot Methods. *Earth and Space Science*, 8(3), 1–15.
677 <https://doi.org/10.1029/2020EA001304>
- 678 IAEA. (2009). Reference sheet for international measurement standards - SMOW Vienna
679 Standard Mean Ocean.
- 680 Johnsen, S. J., Dansgaard, W., & White, J. W. C. (1989). The origin of Arctic precipitation under
681 present and glacial conditions. *Tellus, Series B*, 41 B(4), 452–468.
682 <https://doi.org/10.3402/tellusb.v41i4.15100>
- 683 Jouzel, J., Stievenard, M., Johnsen, S. J., Landais, A., Masson-Delmotte, V., Sveinbjornsdottir,
684 A., et al. (2007). The GRIP deuterium-excess record. *Quaternary Science Reviews*, 26(1–2),
685 1–17. <https://doi.org/10.1016/j.quascirev.2006.07.015>
- 686 Keeling, C. D. (1958). The concentration and isotopic abundances of atmospheric carbon dioxide
687 in rural areas. *Geochimica et Cosmochimica Acta*, 13, 322–324. Retrieved from
688 <papers2://publication/uuid/A28C5407-A4A1-4D85-9BA9-589DE73CD49C>
- 689 Kljun, N., Calanca, P., Rotach, M. W., & Schmid, H. P. (2015). A simple two-dimensional
690 parameterisation for Flux Footprint Prediction (FFP). *Geoscientific Model Development*,
691 8(11), 3695–3713. <https://doi.org/10.5194/gmd-8-3695-2015>
- 692 Lee, X., Kim, K., & Smith, R. (2007). Temporal variations of the 18O/16O signal of the whole-
693 canopy transpiration in a temperate forest. *Global Biogeochemical Cycles*, 21(3), 1–12.
694 <https://doi.org/10.1029/2006GB002871>
- 695 LeGrande, A. N., & Schmidt, G. A. (2006). Global gridded data set of the oxygen isotopic
696 composition in seawater. *Geophysical Research Letters*, 33(12), 1–5.
697 <https://doi.org/10.1029/2006GL026011>
- 698 Luz, B., Barkan, E., Yam, R., & Shemesh, A. (2009). Fractionation of oxygen and hydrogen
699 isotopes in evaporating water. *Geochimica et Cosmochimica Acta*, 73(22), 6697–6703.
700 <https://doi.org/10.1016/j.gca.2009.08.008>
- 701 Markle, B. R., Steig, E. J., Roe, G. H., Winckler, G., & McConnell, J. R. (2018). Concomitant
702 variability in high-latitude aerosols, water isotopes and the hydrologic cycle. *Nature*
703 *Geoscience*, 11(11), 853–859. <https://doi.org/10.1038/s41561-018-0210-9>
- 704 Merlivat, L., & Coantic, M. (1975). Study of mass transfer at the air-water interface by an
705 isotopic method. *Journal of Geophysical Research*, 80(24), 3455–3464.
706 <https://doi.org/10.1029/jc080i024p03455>
- 707 Merlivat, Liliane. (1978). Molecular diffusivities of H₂¹⁶O, HD¹⁶O, and H₂¹⁸O in gases.
708 *The Journal of Chemical Physics*, 69(6), 2864–2871.
- 709 Merlivat, Liliane, & Jouzel, J. (1979). Global climatic interpretation of the deuterium-oxygen 18

- 710 relationship for precipitation. *Journal of Geophysical Research: Oceans*, 84(C8), 5029–
711 5033.
- 712 NOAA. (2019). Bermuda 1 arc-second Coastal Digital Elevation Model. Retrieved from
713 [https://www.ncei.noaa.gov/metadata/geoportal/rest/metadata/item/gov.noaa.ngdc.mgg.dem:
714 5010/html](https://www.ncei.noaa.gov/metadata/geoportal/rest/metadata/item/gov.noaa.ngdc.mgg.dem:5010/html)
- 715 Pfahl, S., & Sodemann, H. (2014). What controls deuterium excess in global precipitation?
716 *Climate of the Past*, 10(2), 771–781. <https://doi.org/10.5194/cp-10-771-2014>
- 717 Pfahl, Stephan, & Wernli, H. (2009). Lagrangian simulations of stable isotopes in water vapor:
718 An evaluation of nonequilibrium fractionation in the Craig-Gordon model. *Journal of
719 Geophysical Research Atmospheres*, 114(20), 1–12. <https://doi.org/10.1029/2009JD012054>
- 720 Pfahl, Stephan, & Wernli, H. (2008). Air parcel trajectory analysis of stable isotopes in water
721 vapor in the eastern Mediterranean. *Journal of Geophysical Research Atmospheres*,
722 113(20), 1–16. <https://doi.org/10.1029/2008JD009839>
- 723 Risi, C., Noone, D., Frankenberg, C., & Worden, J. (2013). Role of continental recycling in
724 intraseasonal variations of continental moisture as deduced from model simulations and
725 water vapor isotopic measurements. *Water Resources Research*, 49(7), 4136–4156.
726 <https://doi.org/10.1002/wrcr.20312>
- 727 Risi, C., Galewsky, J., Reverdin, G., & Brient, F. (2019). Controls on the water vapor isotopic
728 composition near the surface of tropical oceans and role of boundary layer mixing
729 processes. *Atmospheric Chemistry and Physics*, 19(19), 12235–12260.
730 <https://doi.org/10.5194/acp-19-12235-2019>
- 731 Rozanski, K., Araguás-Araguás, L., & Gonfiantini, R. (1993). Isotopic Patterns in Modern
732 Global Precipitation. *Geophysical Monograph*, 78, 1–36.
733 <https://doi.org/10.1029/gm078p0001>
- 734 Sodemann, H., Schwierz, C., & Wernli, H. (2008). Interannual variability of Greenland winter
735 precipitation sources: Lagrangian moisture diagnostic and North Atlantic Oscillation
736 influence. *Journal of Geophysical Research Atmospheres*, 113(3), 1–17.
737 <https://doi.org/10.1029/2007JD008503>
- 738 Sodemann, Harald, & Läderach, A. (2021). WaterSip. Retrieved from
739 <https://wiki.uib.no/gfi/index.php/WaterSip>
- 740 Steen-Larsen, H. C., Masson-Delmotte, V., Sjolte, J., Johnsen, S. J., Vinther, B. M., Bréon, F.
741 M., et al. (2011). Understanding the climatic signal in the water stable isotope records from
742 the NEEM shallow firn/ice cores in northwest Greenland. *Journal of Geophysical Research
743 Atmospheres*, 116(6), 1–20. <https://doi.org/10.1029/2010JD014311>
- 744 Steen-Larsen, H. C., Sveinbjörnsdóttir, A. E., Peters, A. J., Masson-Delmotte, V., Guishard, M.
745 P., Hsiao, G., et al. (2014). Climatic controls on water vapor deuterium excess in the marine
746 boundary layer of the North Atlantic based on 500 days of in situ, continuous
747 measurements. *Atmospheric Chemistry and Physics*, 14(15), 7741–7756.
748 <https://doi.org/10.5194/acp-14-7741-2014>
- 749 Steen-Larsen, H. C., Sveinbjörnsdóttir, A. E., Jonsson, T., Ritter, F., Bonne, J. -L., Masson-
750 Delmotte, V., et al. (2015). Moisture sources and synoptic to seasonal variability of North
751 Atlantic water vapor isotopic composition. *Journal of Geophysical Research Atmospheres*,
752 120. <https://doi.org/10.1002/2015JD023234>
- 753 Stewart, M. K. (1975). Stable isotope fractionation due to evaporation and isotopic exchange of
754 falling waterdrops: Applications to atmospheric processes and evaporation of lakes. *Journal
755 of Geophysical Research*, 80(9), 1133–1146. <https://doi.org/10.1029/jc080i009p01133>

- 756 Stull, R. B. (1997). *An Introduction to Boundary Layer Meteorology*. Springer.
- 757 Thurnherr, I., Kozachek, A., Graf, P., Weng, Y., Bolshiyarov, D., Landwehr, S., et al. (2020).
758 Meridional and vertical variations of the water vapour isotopic composition in the marine
759 boundary layer over the Atlantic and Southern Ocean. *Atmospheric Chemistry and Physics*,
760 20(9), 5811–5835. <https://doi.org/10.5194/acp-20-5811-2020>
- 761 Uemura, R., Matsui, Y., Yoshimura, K., Motoyama, H., & Yoshida, N. (2008). Evidence of
762 deuterium excess in water vapor as an indicator of ocean surface conditions. *Journal of*
763 *Geophysical Research Atmospheres*, 113(19), 1–10. <https://doi.org/10.1029/2008JD010209>
- 764 Uemura, R., Barkan, E., Abe, O., & Luz, B. (2010). Triple isotope composition of oxygen in
765 atmospheric water vapor. *Geophysical Research Letters*, 37(4), 1–4.
766 <https://doi.org/10.1029/2009GL041960>
- 767 UK MET OFFICE. (2005). OSTIA L4 SST Analysis. Ver. 1.0. PO.DAAC.
768 <https://doi.org/https://doi.org/10.5067/GHOST-4FK01>
- 769 Veron, F. (2015). Ocean spray. *Annual Review of Fluid Mechanics*, 47, 507–538.
770 <https://doi.org/10.1146/annurev-fluid-010814-014651>
- 771